ACS NANO

www.acsnano.org

Water in the Electrical Double Layer of Ionic Liquids on Graphene

Qianlu Zheng, Zachary A. H. Goodwin, Varun Gopalakrishnan, Alexis G. Hoane, Mengwei Han, Ruixian Zhang, Nathaniel Hawthorne, James D. Batteas, Andrew A. Gewirth, and Rosa M. Espinosa-Marzal*

Cite This: *ACS Nano* 2023, 17, 9347−9360

Read Online

ACCESS | Metrics & More | Article Recommendations | Supporting Information

ABSTRACT: The performance of electrochemical devices using ionic liquids (ILs) as electrolytes can be impaired by water uptake. This work investigates the influence of water on the behavior of hydrophilic and hydrophobic ILs—with ethylsulfate and tris(perfluoroalkyl)trifluorophosphate or bis(trifluoromethyl sulfonyl)imide (TFSI) anions, respectively—on electrified graphene, a promising electrode material. The results show that water uptake slightly reduces the IL electrochemical stability and significantly influences graphene's potential of zero charge, which is justified by the extent of anion depletion from the surface. Experiments confirm the dominant contribution of graphene's quantum capacitance (C_Q) to the total interfacial capacitance (C_{int}) near the PZC, as expected from theory. Combining theory and experiments reveals that the hydrophilic IL efficiently screens surface charge and exhibits the largest double layer capacitance ($C_{IL} \sim 80\ \mu F\ cm^{-2}$), so that C_Q governs the charge stored. The hydrophobic ILs are less efficient in charge screening and thus exhibit a smaller capacitance ($C_{IL} \sim 6{-}9\ \mu F\ cm^{-2}$), which governs C_{int} already at small potentials. An increase in the total interfacial capacitance is observed at positive voltages for humid TFSI-ILs relative to dry ones, consistent with the presence of a satellite peak. Short-range surface forces reveal the change of the interfacial layering with potential and water uptake owing to reorientation of counterions, counterion binding, co-ion repulsion, and water enrichment. These results are consistent with the charge being mainly stored in a ∼2 nm-thick double layer, which implies that ILs behave as highly concentrated electrolytes. This knowledge will advance the design of IL-graphene-based electrochemical devices.

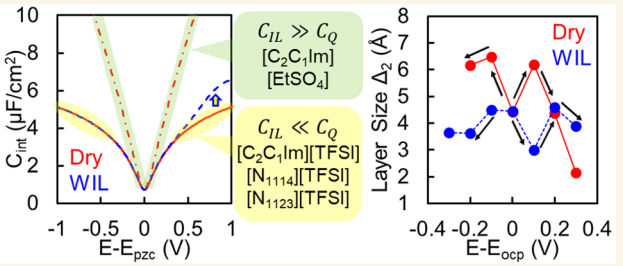

KEYWORDS: *graphene, ionic liquids, electrical double layer, capacitance, force measurements*

Electrical double layer (EDL) capacitors offer many advantages for energy storage including fast charge/discharge processes, long cycle life, excellent safety, no maintenance, and environmental benefits.[1] Among the promising graphitic-based materials for supercapacitor electrodes,[2−4] graphene exhibits very good conductivity,[5] excellent chemical stability, high flexibility and mechanical strength,[5] and high specific area (2630 $m^2\ g^{-1}$)[6] and a theoretical capacity of up to 550 F g^{-1}.[7] On the other hand, the electrolyte's composition at electrified interfaces is critical in determining the stored charge in the EDL as well as the electrochemical reactivity and stability. Ionic liquids (ILs) are promising electrolytes for energy storage due to their low volatility, high thermal and electrochemical stability, non-flammability, and high charge density, with the theoretical capability of outperforming aqueous and organic electrolytes.[8] Several studies show that the capacitance of porous graphene-based electrodes can achieve 100s of F g^{-1} with ILs. However, specific energy stored in graphene/IL supercapacitors still lags behind Li ion batteries,[9,10] which calls for a better understanding of the properties of the electrified interface and the stored charge in this system.

To the best of the authors' knowledge, three previous works have experimentally investigated the interfacial capacitance of pure imidazolium ILs on graphene.[11−13] The total interfacial capacitance (C_{int}) has been modeled as the IL contribution (C_{IL}) connected in series with the quantum capacitance of graphene (C_Q), which can be expressed as $1/C_{int} = 1/C_{IL} + 1/C_Q$. This model assumes that the two capacitances can be treated independently, and hence, it ignores their complex

Received: February 6, 2023
Accepted: May 5, 2023
Published: May 10, 2023

https://doi.org/10.1021/acsnano.3c01043
ACS Nano 2023, 17, 9347−9360

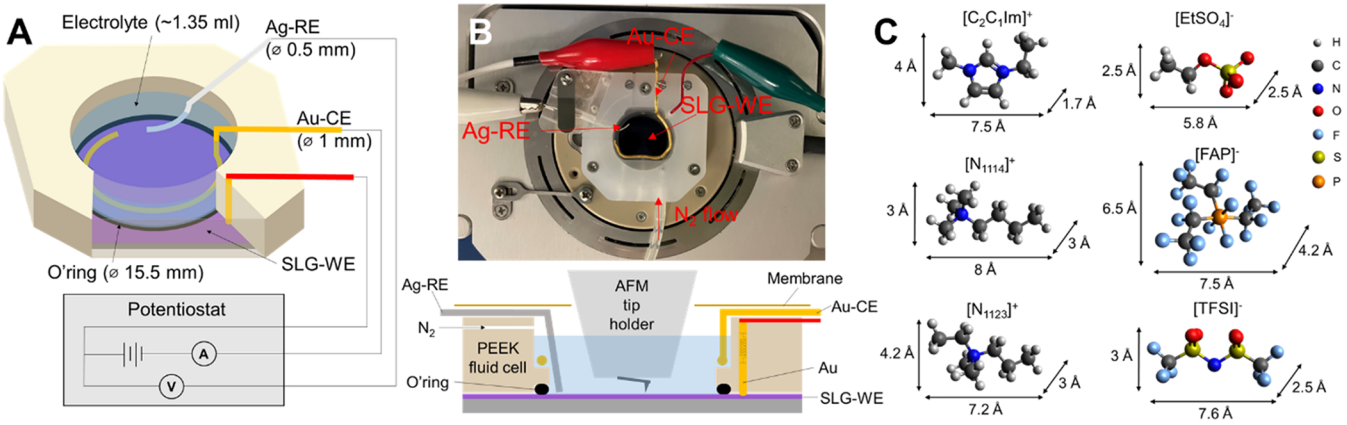

Figure 1. Schematics of (A) electrochemical (EC) cell and (B) AFM EC cell with single layer graphene (SLG) as working electrode (WE), Au wire as counter electrode (CE) and Ag wire as reference electrode (RE). (C) Molecular structure of IL cations and anions. Size was determined by the software Avogadro 1.2.0 using MMFF94 as the force field for energy minimization.

Table 1. Water Uptake by ILs at 33% RH and Contact Angle of the ILs on Graphene at 0% RH ($\theta_{0\%}$) and at 33% RH ($\theta_{33\%}$)[a]

		$[C_2C_1Im][EtSO_4]$	$[C_2C_1Im][FAP]$	$[C_2C_1Im][TFSI]$	$[N_{1114}][TFSI]$	$[N_{1123}][TFSI]$
water at 33% RH	mol/mol	1.51 ± 0.01	0.08 ± 0.05	0.13 ± 0.02	0.055 ± 0.009	0.052 ± 0.006
	ppm	103161 ± 761	2582 ± 1616	5944 ± 919	2491 ± 409	2536 ± 272
contact angle	$\theta_{0\%}$	52.7	34.5	38.2	28.4	29.6
	$\theta_{33\%}$	36.0	20.7	36.1	23.3	32.7
	$\Delta\theta$	−16.7	−13.8	−2.1	−5.1	+3.1

[a]Water at 33% RH in units of mole ratio of water to IL and in ppm, and contact angle at 0% RH ($\theta_{0\%}$) and at 33% RH ($\theta_{33\%}$), where $\Delta\theta = \theta_{33\%} - \theta_{0\%}$.

interdependency, other than the distribution of the total potential drop between them.[14] The two capacitors in series store the same charge, which is mainly dictated by the component with the smallest capacitance. C_Q is V-shaped with a nonzero minimum at the Dirac point and a linear increase with potential.[13] At voltages close to the potential of zero charge, $C_Q \ll C_{IL}$ and hence, $C_{int} \approx C_Q$. Based on this model, Xia et al.[13] assumed a constant C_{IL} to extract C_Q from differential capacitance measurements at the IL/graphene interface. Deviations of the measured C_Q from theoretical predictions were observed, however. Although not yet reported, it can be expected that, at sufficiently large voltages, $C_Q \gg C_{IL}$, and thus, C_{int} should be determined by C_{IL}, while at intermediate voltages, there should be an influence of both quantum capacitance and the IL capacitance. This work examines these conditions as well.

When ILs are exposed to ambient air, they absorb water[15] and the amount of absorbed water increases with the hydrogen-bonding ability of the IL, typically of the anion, with water.[15−17] The presence of water impurities can be detrimental to the performance of EDL capacitors because it can discharge the capacitor at voltages that turn on water electrolysis. In addition, if ILs are used as inert electrolytes for electrocatalytic reactions, water electrolysis can obscure any targeted electrochemical reaction at the electrode. Hence, understanding the effect of water on the double layer is essential to evaluate the electrochemical performance of the electrolyte. Simulations by Feng et al.[18] showed that small amounts of water should not disturb the structure of the IL in the EDL and that water has a preference to reside in locations with more space and higher electric field, and overall, water molecules prefer positive electrodes because of their favorable interactions with anions. This asymmetry in the electrical response gives rise to a satellite peak in the differential capacitance at positive potentials, as clearly shown by mean-field theory.[19] It was also justified later by Bi et al.[20] that, perhaps counterintuitively, ILs with hydrophilic anions are better than hydrophobic anions at keeping water away from negative electrodes. MD simulations of the IL-graphene interface with water by Docampo-Alvarez et al.[21] showed that water was depleted at neutral and negatively charged interfaces, but an accumulation happened at positive interfaces, because of the favorable interaction with anions.

The effect of water on the IL/graphene interfacial capacitance and on the interfacial structure has not been experimentally studied yet to the best of the authors' knowledge. This work investigates the influence of water on the capacitance of the graphene/IL interface and compares capacitance measurements and calculations by theory to the interfacial structure as inferred from atomic force microscopy (AFM) force measurements. We have selected ILs with the same imidazolium cation and three different anions, based on the expected influence of the anion on the interaction with water, as well as three ILs with the same anion and three different cations to also examine the effect of water on the specific adsorption of the cation on graphene. Overall, this work improves our understanding of the charge stored in the EDL of ILs on graphene.

RESULTS

Single-layer graphene (SLG) synthesized by chemical vapor deposition and deposited on a silicon oxide substrate (Graphenea, Spain) was annealed under 450 °C for 4 h in dry nitrogen flow. The Raman spectrum of SLG on SiO_2 substrates and images taken by AFM are shown in the Supporting Information (SI), Figure S1. Electrochemical and

https://doi.org/10.1021/acsnano.3c01043
ACS Nano 2023, 17, 9347−9360

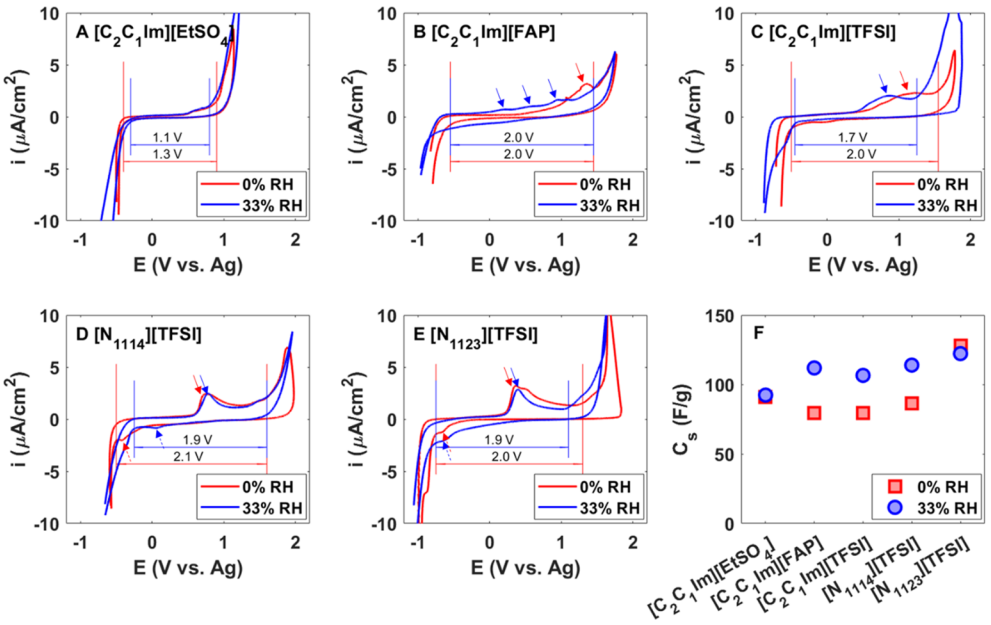

Figure 2. CVs of (A) $[C_2C_1Im][EtSO_4]$, (B) $[C_2C_1Im][FAP]$, (C) $[C_2C_1Im][TFSI]$, (D) $[N_{1114}][TFSI]$, and (E) $[N_{1123}][TFSI]$ on graphene at 0% (red) and 33% RH (blue). Scan rate: 10 mV/s. The ESW is shown in each plot. A current cutoff of 1−2 $\mu A/cm^2$ was selected to determine the ESW of the electrolytes. Arrows point at adsorption peaks measured from negative to positive sweep, and dashed arrows point at adsorption peaks measured from positive to negative bias sweep. (F) Calculated specific capacitance in the potential window ~ ±0.5 V; corresponding CVs are shown in Figure S5. The error bars give the standard deviation among multiple cycles, but they are smaller than the marker size and therefore not visible.

AFM force measurements were performed in a three-electrode-cell where the potential of the working electrode (graphene) was controlled with respect to a reference Ag electrode (E vs. Ag) (Figure 1A,B). The experimental setup is described in detail in the Materials and Methods section.

Ethyl sulfate (abbrev. $[EtSO_4]^-$), tris(perfluoroalkyl)-trifluorophosphate (abbrev. $[FAP]^-$), and bis-(trifluoromethylsulfonyl)imide (abbrev. $[TFSI]^-$) were selected to investigate the influence of the anion with the same cation, 1-ethyl-3-methyl imidazolium (abbrev. $[C_2C_1Im]^+$). In addition, butyltrimethylammonium (abbrev. $[N_{1114}]^+$), ethyl-dimethylpropylammonium (abbrev. $[N_{1123}]^+$) and $[C_2C_1Im]^+$ were selected to investigate the influence of the cation with the same anion, $[TFSI]^-$. Figure 1C shows the molecular structures of the selected IL ions. Electrochemical and AFM experiments were performed in equilibrium with dry nitrogen (labeled as "dry" condition or 0% relative humidity, RH) and with air at 33% RH. Table 1 shows the average water content in the ILs, as determined from gravimetric measurements in equilibrium at 33% RH. $[C_2C_1Im][EtSO_4]$ is highly hydrophilic, absorbing ~1.51 water molecules per ion pair. The other four ILs contain a much smaller water content (~40 times less in ppm), i.e., they are comparatively very hydrophobic, with hydrophobicity increasing (decreasing water content) in the order, $[C_2C_1Im][TFSI]$ < $[C_2C_1Im]$-$[FAP]$ < $[N_{1114}][TFSI]$ < $[N_{1123}][TFSI]$. The water content at other RHs is displayed in Table S1.

Contact Angle. Table 1 displays the contact angle of dry ILs and of the ILs at 33% RH (water-in-ILs or WILs) on graphene ($\theta_{0\%}$ and $\theta_{33\%}$, respectively). The highest contact angle is measured for dry $[C_2C_1Im][EtSO_4]$, which is the IL with the highest hydrogen bond accepting ability; this has been reported to disfavor wetting of nonpolar surfaces.[22] Despite the expected $\pi-\pi$ interactions between the imidazolium cation and graphene, the contact angle with $[C_2C_1Im][TFSI]$ is larger than with the quaternary ammonium-based ILs (38° vs 28−30°). This could be related to the longer alkyl chain in $[N_{1114}]^+$ and $[N_{1123}]^+$ compared to $[C_2C_1Im]^+$, which favors ordering at a carbon interface.[23]

The presence of water influences the contact angle of hydrophilic and hydrophobic ILs on graphene. Except in the case of $[N_{1123}][TFSI]$, water molecules lead to a decrease of the contact angle ($\Delta\theta$ < 0). Considering that the surface tension of hydrophobic ILs remains fairly unchanged in equilibrium at 33% RH due to their small water content,[24] the decrease of the contact angle implies an increase in the solid−liquid interaction energy, which supports the presence of water at the interface. However, there is no obvious correlation between the water content at 33% RH and the change of the contact angle $\Delta\theta$. The change is very small for all the ILs with $[TFSI]^-$ anions, compared to $[FAP]^-$ and $[EtSO_4]^-$, and hence, these results suggest the role of the anion in influencing the interaction between water and graphene, which is supported by additional results described later.

Cyclic Voltammetry. The voltammograms of the dry ILs and WILs are shown in Figure 2A−E; reference measurements on gold electrodes are shown in Figure S2. Except in the case of $[C_2C_1Im][EtSO_4]$, a prominent peak (see arrows, ~0.5−1.5 V) is observed for dry ILs and WILs when the potential sweeps from negative to positive bias. It suggests that the cations are still at the electrode surface when the surface is positively biased, and hence, it points toward the specific adsorption of the cations on graphene. The presence of water slightly reduces the area below the peak with respect to the baseline (see Figure S3). This indicates that the graphene−cation interaction is weakened by water. Such specific adsorption of the cation does not happen to the same extent in the case of

https://doi.org/10.1021/acsnano.3c01043
ACS Nano 2023, 17, 9347−9360

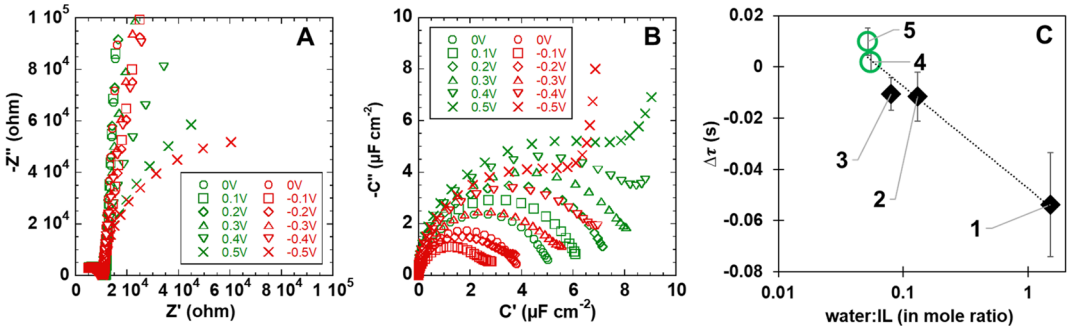

Figure 3. Representative EIS results and time constant of the double layer. (A) Nyquist plot and (B) complex capacitance (Cole−Cole) plots for dry $[C_2C_1Im][EtSO_4]$. The values in the legend are the potentials with respect to the OCP, $\Delta U = E - E_{OCP}$. EIS plots for other ILs and WILs and conditions are shown in Figures S6 and S7. (C) Change of the time constant upon water uptake, $\Delta\tau = \tau_{33\%} - \tau_{0\%} \sim \ln(w)$ for imidazolium ILs (full diamonds) and ammonium ILs (empty circles): 1, $[C_2C_1Im][EtSO_4]$; 2, $[C_2C_1Im][TFSI]$; 3, $[C_2C_1Im][FAP]$; 4, $[N_{1114}][TFSI]$; and 5, $[N_{1123}][TFSI]$. The plot shows average and standard deviation for the time constant values calculated at each potential *E*.

$[C_2C_1Im][EtSO_4]$, presumably due to the hydrogen bonding between anion and cation in this IL.[25]

The electrochemical stability window (ESW) of the ILs is shown in each plot. Despite the high water content, anodic and cathodic limits of $[C_2C_1Im][EtSO_4]$ change only slightly (Figure 2A). This can be justified by the large activation overpotential of water on graphene (Figure S4). In addition, it is possible that, as shown in MD simulations for hydrophilic ILs,[20] the hydrogen bonding between the anion and water[25,26] keeps water out of the EDL at negative potentials. The cyclic voltammetry (CV) of $[C_2C_1Im][EtSO_4]$ was also measured on gold electrodes at various water contents (Figure S2A). Here, the cathodic limit remains almost constant—likely due to the repulsion of the anions, which hydrogen bond with water[25,26]—but the anodic limit decreases gradually and significantly with the increase of the water content. This is consistent with the much higher activity of water on gold compared to water on graphene electrodes, as demonstrated by the reference measurements with aqueous KCl solution (Figure S4). Note several peaks in the CV for water on gold, which may not only reflect concurrent lattice reconstruction, but also gold oxidation and reduction of gold oxide.[27]

Dry hydrophobic ILs exhibit a wider electrochemical stability compared to $[C_2C_1Im][EtSO_4]$ (~2 V vs 1.3 V). For $[C_2C_1Im][TFSI]$ and $[N_{1123}][TFSI]$ on graphene at 33% RH (Figure 2C,E), the CVs show almost no reduction of the cathodic limit, but a slight reduction of the anodic limit, which suggests that water is enriched preferentially at positive potentials, and is consistent with MD simulations of hydrophobic ILs.[18] The reduction of the anodic limit is much smaller for $[N_{1114}][TFSI]$ on graphene electrodes (Figure 2D), and in the case of $[C_2C_1Im][FAP]$, anodic and cathodic limits do not change (Figure 2B). We believe that this is partially justified by the large overpotential of water on graphene (Figure S4), which leads to an ESW of ~2 V in reference measurements with aqueous KCl solution at the same scan rate as the CVs in Figure 2. This is very different from the behavior of the WILs on gold. Here, the cathodic limit of $[C_2C_1Im][TFSI]$ is reduced already at 11% RH and is almost insensitive to the increase in water content at higher RH (Figure S2B). The results are similar for $[N_{1114}][TFSI]$ on gold (Figure S2C), which supports the presence of water also on the negatively charged gold electrodes for these hydrophobic ILs. Overall, the presence of water traces leads to only a small reduction of the ESW of the hydrophobic ILs on graphene, while the decrease in the electrochemical stability window is much more significant on gold electrodes. As discussed above and in Figure S4, the higher activity of water on gold compared to graphene can justify these results.

Figure 2F displays the specific capacitance (C_s) of ILs and WILs determined within the narrow potential range ~ ±0.5 V from CVs at 10 mV/s. In this narrow potential window, the CVs look close to ideal, although subtle adsorption peaks can still be seen for $[C_2C_1Im][TFSI]$ and $[N_{1123}][TFSI]$ with water, and hence, they slightly influence the calculated specific capacitance. For the dry ILs, the specific capacitance of $[N_{1123}][TFSI]$ is the largest (~128 F g^{-1}), followed by $[C_2C_1Im][EtSO_4]$ (~91 F g^{-1}) and $[N_{1114}][TFSI]$ (~86 F g^{-1}), while the specific capacitance of dry $[C_2C_1Im][FAP]$ and $[C_2C_1Im][TFSI]$ is a bit smaller and very similar (~79 F g^{-1}). The influence of water on the capacitance of $[C_2C_1Im][EtSO_4]$ is negligible (~92 F g^{-1}), which is noteworthy considering the large water content. Similarly, the decrease of capacitance is very small for $[N_{1123}][TFSI]$ (~128 F g^{-1}). In contrast, a significant increase of the specific capacitance is observed for $[C_2C_1Im][FAP]$, $[C_2C_1Im][TFSI]$ and $[N_{1114}][TFSI]$ upon equilibration at 33% RH (~41%, 34% and 32% increase, respectively). The increase of the specific capacitance could be justified by the following reasons: (1) water molecules can screen electrostatic interactions between cations and anions and thereby favor surface charge screening by counterions; and (2) water has a larger dielectric constant than ILs,[28] which leads to an increase of dielectric constant at the interface with water enrichment. Indeed, the experimentally observed satellite peak in the double layer capacitance of ILs in the presence of water on gold electrodes,[29] is shown by theory to be due to the increase of the dielectric constant when water accumulates at the electrode surface.[19] Because the presence of water does not influence the specific capacitance of $[C_2C_1Im][EtSO_4]$, for which a high water content is expected, additional competing mechanisms are expected. For example, the high concentration of water at the interface could reduce the counterion concentration and, thereby, overall hinder charge screening. In addition, it is possible that the quantum capacitance of graphene dictates the overall stored charge in this narrow potential range. Electrochemical impedance spectroscopy (EIS) measurements provide more insight into this phenomenon.

https://doi.org/10.1021/acsnano.3c01043
ACS Nano 2023, 17, 9347−9360

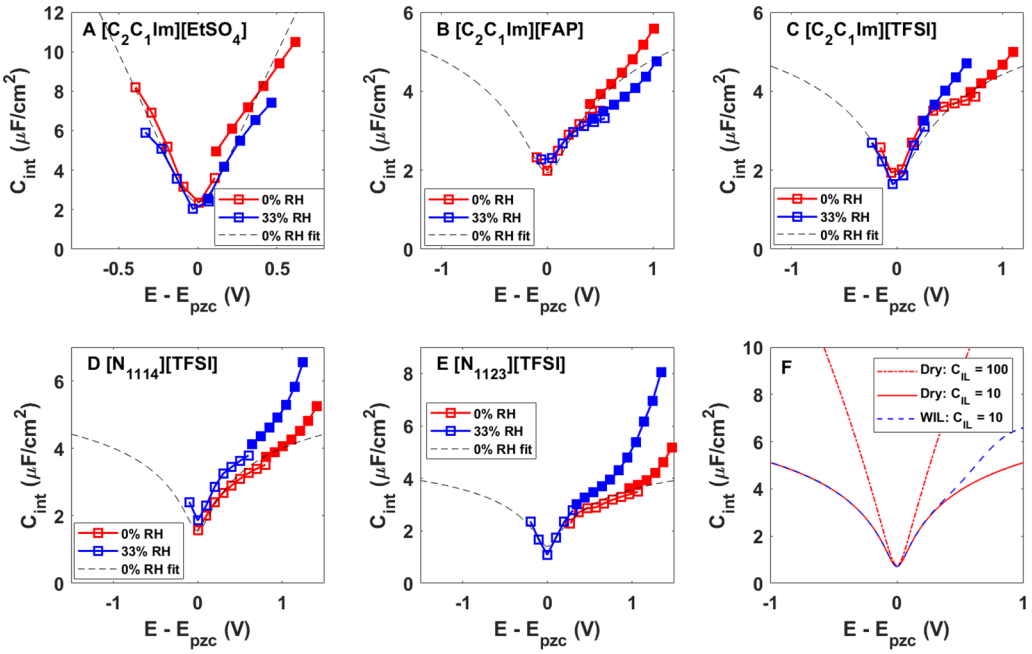

Figure 4. Differential total interfacial capacitance from experiments and theory. (A–E) Total interfacial capacitance (C_{int}) as a function of $E - E_{PZC}$ for dry ILs (red) and WILs (blue) and fitted theoretical data for the dry ILs (black dashed line). Full symbols indicate the measured data upon increasing potential from the OCP, and empty markers represent the measured data points upon decreasing potential from the OCP. The V-shape of the total capacitance is evident close to the PZC for all ILs. The PZC of $[N_{1123}][TFSI]$ and $[N_{1114}][TFSI]$ was determined in separate experiments to be −0.8 and −0.5 V, respectively. Figure S10 shows the same data (C_{int}) but with the potential E in the X-axis to illustrate the shift of the PZC (Figure S9). (F) Theoretical calculations of interfacial capacitance for dry IL with C_{IL} = 10 and 100 μF cm^{-2} and for WILs with C_{IL} = 10 μF cm^{-2}.

Electrochemical Impedance Spectroscopy. The results of EIS measurements are shown in Figures 3, S6 and S7. Nyquist and Cole–Cole plots were examined to understand the behavior of the ILs on graphene electrodes. The vertical line in the Nyquist plots (Figure 3A) and the high-frequency semicircle in the complex capacitance plane (Figure 3B) represent a fast capacitive process resulting from the charging process.[30−32] A fast capacitive process is observed both at positive and negative bias potentials. By fast double layer formation, it is typically understood that the double layer formation time is determined by the bulk resistance of the ILs, whereas other capacitive and Faradaic processes are slower due to the existence of additional barriers at the interface.[30] Such slow processes can generally result from the atomic reconstruction of the electrode surface, ion redistribution within the double layer, specific adsorption of ions, and Faradaic events within the compact layer.[32] While reconstruction of graphene is unlikely, slow dynamics of imidazolium ILs at the graphene/IL interface are likely, as previously reported.[33] Slow capacitive processes at negative potentials are more significant for $[C_2C_1Im][TFSI]$, $[C_2C_1Im][FAP]$ and $[C_2C_1Im][EtSO_4]$ compared to the alkylammonium ILs, and hence, they may be associated with the slow adsorption and reorganization of the imidazolium cation on graphene electrodes.

The differential capacitance was determined by three different methods, which are described in detail in the SI. The three methods led to qualitatively similar results; see example in Figure S8. Hence, we discuss only the model fits to Cole–Cole plots. First, we discuss the potential of zero charge (PZC), which is defined as the potential at which the electrode has no surface free charge. The graphene and IL capacitances are joined in series, and the quantum capacitance of graphene vanishes (becomes extremely small) at charge neutrality. Hence, the potential at PZC (E_{PZC}) is determined at the minimum in the capacitance curves (Figure S9). For the two alkylammonium ILs, additional measurements were performed up to more negative potentials (Figure 4) to enable the determination of the PZC; see Figure S10.

The potential at PZC is summarized in Table 2. The PZC is located at ∼0 V for $[C_2C_1Im][EtSO_4]$ and at a negative potential for the four hydrophobic ILs, decreasing (becoming more negative) in the order $[C_2C_1Im][FAP]$ > $[C_2C_1Im][TFSI]$ > $[N_{1114}][TFSI]$ > $[N_{1123}][TFSI]$. A negative PZC reflects the n-type doping state of graphene, and it has been reported for graphene with $[C_4C_1Im][PF_6]$[13] and $[C_2C_1Im][TFSI]$,[11] previously. Note that graphene on a SiO_2 substrate becomes slightly p-doped via charge transfer due to the presence of oxygen dangling bonds on the substrate surface.[34] Hence, the n-doping of graphene can be attributed to the interaction between ILs and graphene. The PZC is most negative for the ILs with TFSI anions, followed by $[C_2C_1Im][FAP]$ and $[C_2C_1Im][EtSO_4]$. When water is present, the minimum of the interfacial capacitance shifts to the right (i.e., it becomes less negative) for all the ILs except $[C_2C_1Im]$-

Table 2. Working electrode potential E (V vs. Ag) at the PZC of graphene

E_{PZC} [E vs. Ag]	0%	33%	$E_{PZC,33\%} - E_{PZC,0\%}$
$[C_2C_1Im][EtSO_4]$	−0.03	+0.08	+0.11
$[C_2C_1Im][FAP]$	−0.20	−0.28	−0.08
$[C_2C_1Im][TFSI]$	−0.36	0.03	+0.39
$[N_{1114}][TFSI]$	−0.47	−0.38	+0.09
$[N_{1123}][TFSI]$	−0.82	−0.35	+0.47

https://doi.org/10.1021/acsnano.3c01043
ACS Nano 2023, 17, 9347−9360

[FAP]. Because water molecules favor p-type doping of graphene,[35] it is possible that the surface enrichment of water is responsible for the positive shift of the PZC, as seen for $[C_2C_1Im][EtSO_4]$ (from ~0 V to ~+0.1 V). However, for $[C_2C_1Im][FAP]$, the PZC becomes more negative (−0.2 V at 0% vs −0.28 V at 33% RH), which points at a different (additional) mechanism that will be discussed later.

The total interfacial capacitance C_{int} with respect to $\Delta E_{PZC} = E - E_{PZC}$ is displayed in Figure 4A−E for the dry ILs (red squares) and WILs (blue squares). For $[C_2C_1Im][EtSO_4]$, C_{int} exhibits a close-to V-shape and varies between ~2 and 10 μF cm^{-2} over a small potential window of ~1 V (Figure 4A). For the other dry ILs (Figure 4B−F), C_{int} varies between 2 and 5 μF cm^{-2} over a wider potential window of 1.4−1.6 V and exhibits a more complicated potential dependence. Except in the case of $[C_2C_1Im][EtSO_4]$, EIS experiments in Figure 4 mainly probe the positive charge of graphene.

To understand the differences between these curves, we performed theoretical fits to C_{int} based on the quantum capacitance of graphene[13] and models for the IL capacitance.[36,37] The full details of the calculation are shown in the SI, but the approach is to find the IL capacitance (C_{IL}) at large potentials, where the total capacitance is dominated by the IL, as the graphene capacitance (C_Q) is a universal value determined by the Fermi velocity of the Dirac cone at large potentials. Close to the PZC, C_{int} is dominated by C_Q, where we find it necessary to include a contribution from charge defects, as described in the SI text. In Table 3, we show the extracted values of C_{IL} and charge defect concentration (n^*). The dashed lines in Figure 4A−E give the fitted curves for dry ILs.

Table 3. Differential Capacitance of the dry ILs (C_{IL}) and Charge Defect Concentration (n^*) Obtained from Fits of the Theory to the Measured Total Interfacial Capacitance

	C_{IL} [μF cm^{-2}]	n^* [10^{12} cm^{-2}]
$[C_2C_1Im][EtSO_4]$	80	0.7
$[C_2C_1Im][FAP]$	9	0.9
$[C_2C_1Im][TFSI]$	7	0.8
$[N_{1114}][TFSI]$	7	0.5
$[N_{1123}][TFSI]$	6	0.5

We find a large capacitance of 80 μF cm^{-2} for $[C_2C_1Im][EtSO_4]$, which means the quantum capacitance dominates in this case for all the studied potentials, giving rise to the close-to ideal V-shape. In Figure 4F, we show a theoretical calculation with large IL capacitance (100 μF cm^{-2}), which displays this ideal V-shape. In contrast, for the hydrophobic ILs, we find capacitance values in the range of 5−9 μF cm^{-2} and charged defect concentrations of 0.5−0.9 × 10^{12} cm^{-2}. For such values, the quantum capacitance of graphene only dominates close to the PZC, giving rise to a small V-shape at small potentials. This V-shape quickly starts to flatten out, as the IL capacitance becomes the limiting contribution, which gives rise to flattened wings in the total capacitance curves. An example of which from the theory is shown in Figure 4F. Overall, the results for dry ILs are consistent with previous experiments.[11,38]

Next, we turn to describing the effect of water on the total interfacial capacitance. In Figure 4, the results for 33% RH are shown alongside the dry curves. All curves are aligned at 0 in the X-axis using $E - E_{PZC}$, which ensures a direct comparison. For $[C_2C_1Im][EtSO_4]$, there is very little effect from the addition of a substantial amount of water. This suggests that the differential capacitance of $[C_2C_1Im][EtSO_4]$ at 33% RH is still large. It is difficult to exactly determine how much the IL capacitance could be changing for $[C_2C_1Im][EtSO_4]$ because the total capacitance is dominated by the graphene contribution, meaning extracting accurate values for the IL contribution is difficult; values between 50 and 200 μF cm^{-2} all work reasonably well. For ILs with the $[TFSI]^-$ anion, C_{int} is practically identical near the PZC. But at large positive voltages, the 33% RH curves all increase above the dry IL curves. This increase in the capacitance can presumably be attributed to the water-satellite peak that was recently predicted by Budkov et al.[19] Note that the effect of water on the differential capacitance becomes more significant with increase in positive potential, as the slope of the interfacial capacitance increases and deviates from the linear trend of C_Q. In Figure 4F, we show an example curve of the expected effect of the water satellite peak from theory (details of the calculation are described in the SI), which qualitatively agrees well with the results for ILs that have $[TFSI]^-$ anions.

For $[C_2C_1Im][FAP]$, the results are different. Here, we find that the total capacitance close to the PZC is similar for dry and 33% RH, but at large potentials the dry IL appears to have slightly larger values. This different behavior is concurrent with the PZC becoming more negative for $[C_2C_1Im][FAP]$ at 33% RH, which is the opposite trend compared to the ILs with $[TFSI]^-$ anion. The significant decrease of the contact angle (Table 1) supports the presence of water at the interface, and the multiple subtle but broad adsorption peaks at 33% RH (see arrows in Figure 2B) are consistent with the complexity of this interface. Further, we note that the increase of the specific capacitance C_s of $[C_2C_1Im][FAP]$ upon water uptake (Figure 2B) is at odds with the results presented here. This might be due to the high scan rate used in CV (10 mV s^{-1}) compared to the much slower change of potential in EIS (~0.3 mV s^{-1}).

The time constant (τ) for the double layer formation was obtained from modeling C_{int}; see model description and results in Figure S11. For the dry ILs, the shortest time constants ($\tau_{0\%}$) are obtained for $[C_2C_1Im][FAP]$ ($\tau_{0\%}$ ~36 ± 11 ms), followed by $[N_{1123}][TFSI]$ (~45 ± 11 ms), $[C_2C_1Im][TFSI]$ (~63 ± 17 ms), and $[N_{1114}][TFSI]$ (~83 ± 31 ms), and the longest time constant is obtained for $[C_2C_1Im][EtSO_4]$ (~129 ± 46 ms); the standard deviation results from the potential dependence of the time constant. While no correlation is found between the viscosity of dry ILs and WILs and the time constant, there is a quasi-linear correlation between the average time constant and the natural logarithm of the water content, w ($\Delta\tau = \tau_{33\%} - \tau_{0\%} \sim \ln(w)$), as shown in Figure 3C. This plot shows that the water content can reduce the time constant for the imidazolium ILs (full diamonds), but it slightly increases the time constant for the alkylammonium ILs (empty circles).

It is noteworthy that the time constant during charging does not scale with the viscosity of dry ILs and WILs. While deciphering the origin of these results is out of the scope of this work, we propose various mechanisms that could be involved. First, note that τ was obtained from fits to the total interfacial capacitance, and hence, these results include not only the temporal changes of the double layer in the liquid but also the response of the graphene electrode. It is thus possible that ion rearrangements at each potential are coupled with the evolution of the doping state of graphene. The latter, in turn, modifies the double layer structure, so that the time constant includes the coupled interfacial effects in the liquid

https://doi.org/10.1021/acsnano.3c01043
ACS Nano 2023, 17, 9347−9360

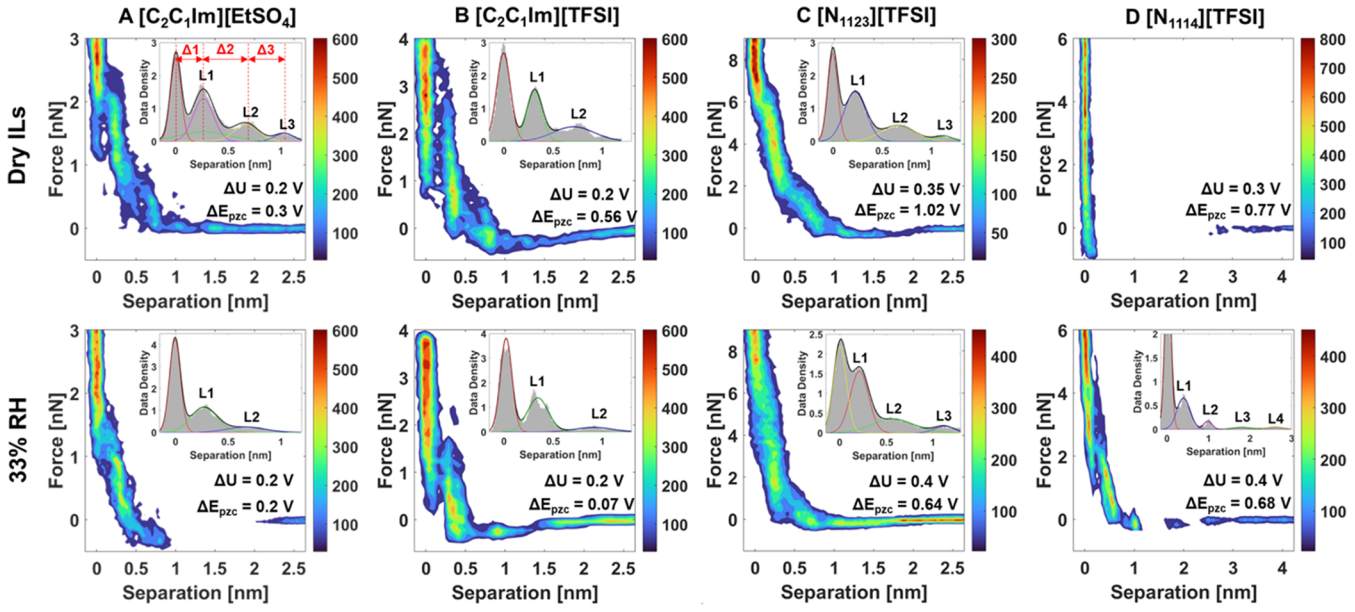

Figure 5. Representative heatmaps of force curves for (A) $[C_2C_1Im][EtSO_4]$, (B) $[C_2C_1Im][TFSI]$, (C) $[N_{1123}][TFSI]$ and (D) $[N_{1114}][TFSI]$ at $\Delta U > 0$. The potential is given with respect to the OCP ($\Delta U = E - E_{OCP}$) and to the PZC of graphene (ΔE_{PZC}). All conditions correspond to $\Delta E_{PZC} > 0$. The jump-in hinders resolving the interfacial structure for $[C_2C_1Im][FAP]$ at several conditions, and hence, the results are not discussed. The insets show the density profiles of the separation to identify the IL layers, and to determine the layer size (Δ). No layers are detected in D, and hence, there is no histogram for $[N_{1114}][TFSI]$ at 0% RH. Note that layers may form on the graphene surface, however, the attractive interaction between tip and surface prevents these layers from being detected.

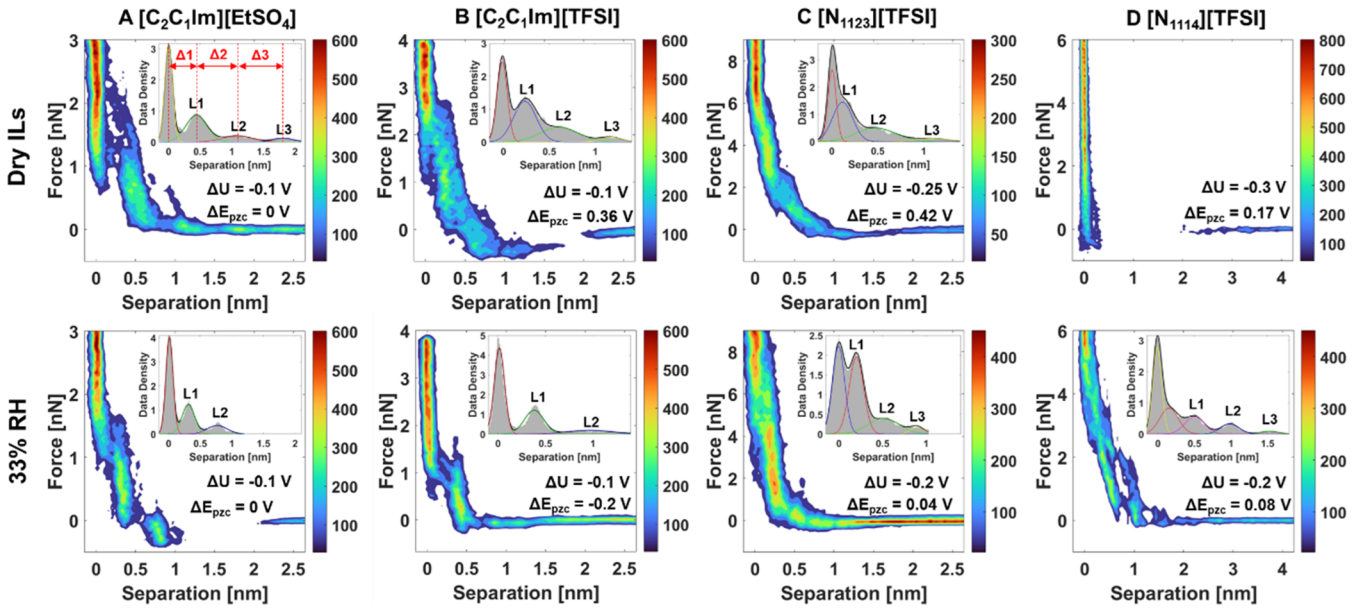

Figure 6. Representative heatmaps of force curves for (A) $[C_2C_1Im][EtSO_4]$, (B) $[C_2C_1Im][TFSI]$, (C) $[N_{1123}][TFSI]$, and (D) $[N_{1114}][TFSI]$ at $\Delta U < 0$. The potential is given with respect to the OCP ($\Delta U = E - E_{OCP}$) and to the PZC of graphene (ΔE_{PZC}). Here, ΔE_{PZC} is smaller than in Figure 5 but positive, except in case of $[C_2C_1Im][TFSI]$ at 33% RH. The insets show the density profiles of the separation to identify the IL layers, and to determine the layer size (Δ). No layers are detected in (D) at 0% RH, and hence, there is no histogram.

and solid. In the case of $[C_2C_1Im][EtSO_4]$, for which doping is irrelevant but it has the longest time constant, it is possible that the hydrogen bonding between cation and anion[39] slows down the rearrangement of the ions in response to the applied potential. Water is known to weaken hydrogen bonding between cation and anion in $[C_2C_1Im][EtSO_4]$,[40] justifying the shorter time constant for the rearrangement of the EDL. The effect of water on reducing the time constant of the hydrophobic imidazolium ILs also points at the role of water in screening anion−cation interactions and thereby facilitating ion rearrangements. This is opposite to the increase of the time constant observed for the alkylammonium ILs, which might result from solvophobic interactions. Here, the presence of water could strengthen anion−cation interactions, which would slow down their rearrangements upon a change of potential. Dynamic studies of the EDL would be needed to provide more insight into this specific question.

https://doi.org/10.1021/acsnano.3c01043
ACS Nano 2023, 17, 9347−9360

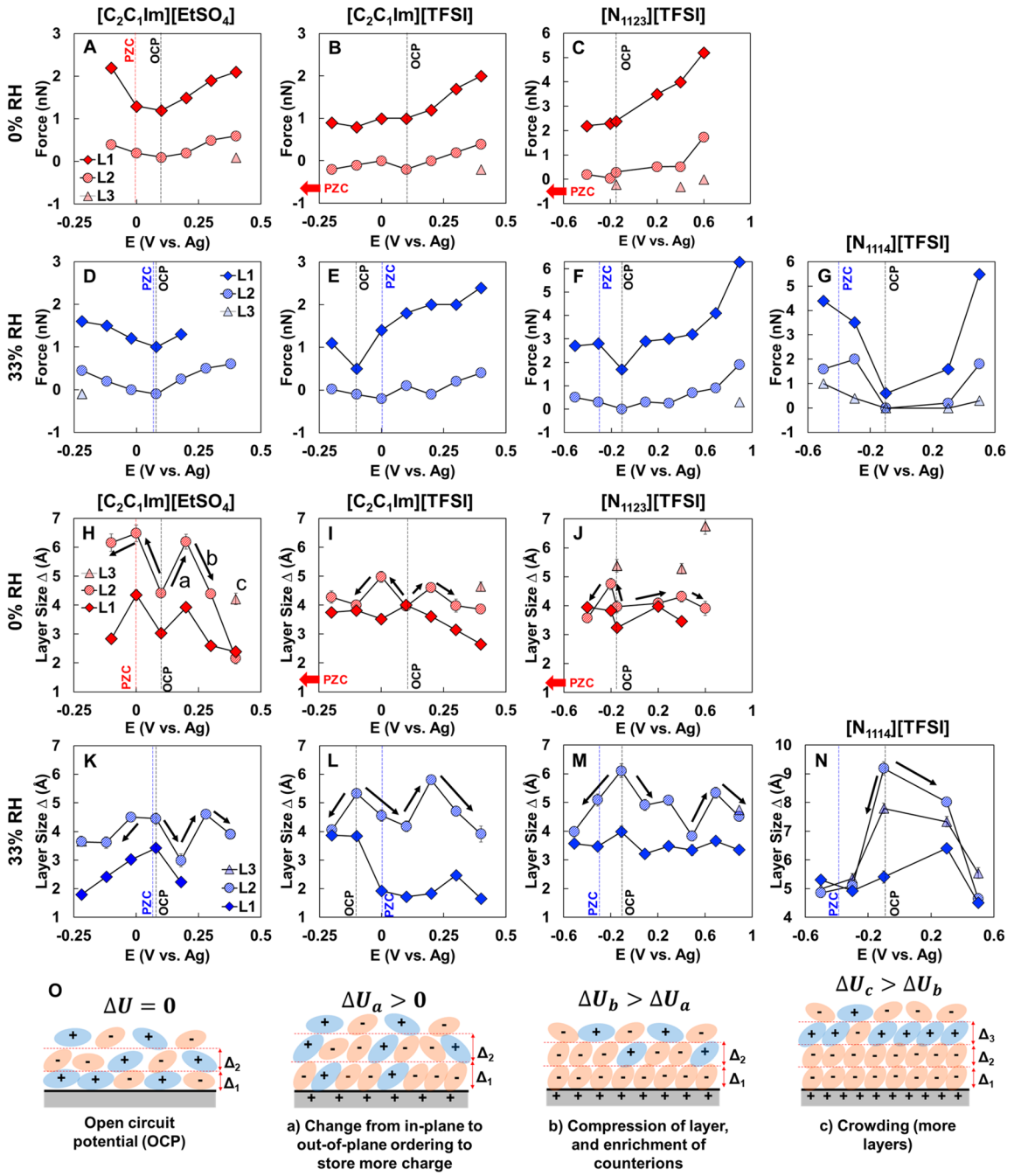

Figure 7. Analysis of the interfacial layers from force–distance curves. (A–G) Rupture force in response to graphene potential (E in V vs. Ag) in (A–C) dry ILs and (D–G) WILs. (H–N) Layer size in response to graphene potential (E in V vs. Ag) in (H–J) dry ILs and (K–N) WILs. L_1 is not resolved at high potentials for $[C_2C_1Im][EtSO_4]$ at 33% RH, likely because the rupture force is higher than the maximum value applied. The red/blue dash lines give E_{PZC} of the dry ILs (red) and WILs (blue), and the black dash lines display E_{OCP}; see the different scale of the Y-axis in (C). The error bars give the square root of the variance of the Gaussian distributions representing the density profile of L_1 and L_2. The error bar is smaller than the marker size and therefore not always visible. The results for $[N_{1114}][TFSI]$ at 0% RH are not shown because the force is attractive, and hence, it is not sensitive to the interfacial structure. Note that the absolute value of the force cannot be compared across ILs and humidity conditions because the measurements were performed with different tips. (O) Schematics showing change of layering behavior with potential for dry ILs.

Force–Distance Curves. Force–distance curves were measured on graphene with a silicon tip at selected potentials within the ESW of the electrolyte. Figures 5 and 6 show representative 2D heatmaps of force–distance curves of dry ILs and WILs at selected positive and negative bias potentials with respect to the OCP ($\Delta U = E - E_{OCP}$), respectively. A total of 64 force curves were measured at each potential, but two different types of force curves were often observed at the same conditions, reflecting a nonuniform interfacial structure, perhaps arising from charge puddles on the graphene surface.[41,42] Previous works have reported the existence of in-plane domains of ILs on graphite, which might be responsible for the two types of force–distance curves.[43] Here, we discuss the heatmaps corresponding to the most

https://doi.org/10.1021/acsnano.3c01043
ACS Nano 2023, 17, 9347–9360

frequent interfacial structure at each experimental condition. Each heatmap includes 20−40 force curves. The force between the tip and graphene results from the solvation force with an oscillatory component arising from the order of the ions in layers close to the graphene surface, electrostatic interaction between the charged surfaces, as well as van der Waals force.[44] The tip-graphene force varies with applied potential, which is associated with the varying composition of the solvation (interfacial) layers, the change of the electrostatic force, and the screening of the surface charge by ions. Furthermore, at any given potential, the force−distance curves significantly change when traces of water molecules are present in the liquid, even for the most hydrophobic ILs. For example, the force in dry $[N_{1114}][TFSI]$ is strongly attractive, whereas it is repulsive at 33% RH. For $[C_2C_1Im][EtSO_4]$, the presence of water at the interface converts the repulsive interaction between tip and graphene into an attractive force.

The discrete steps in the force−distance curves result from the rupture of the layers of IL ions with the AFM tip.[44,45] Note that the position of the hard wall is unknown, and hence, it is possible that the IL layers that are most strongly bound to graphene are not ruptured by the tip, especially at the highest potentials. We call L_1 the layer closest to the hard wall, and the increasing index (L_2, L_3) indicates the increasing distance from the hard wall. The rupture force decreases with distance from the surface ($F_{L1} > F_{L2} > F_{L3}$). To compare the interfacial structure across conditions, 1D histograms of the tip−surface separation were constructed (see inset in each heatmap), and multiple Gaussian distributions were fit to the histograms. The layer size (Δ) gives the distance between the mean value of each Gaussian distribution (see Δ_1, Δ_2 and Δ_3 in the inset of Figure 5A). The values of the layer size and the corresponding rupture force are summarized in Figure 7. Both the applied potential and the water content led to variations of the number of layers detected, the rupture force and/or the layer thickness.

Figure 7A−C shows the variation of the rupture force with potential for dry ILs. For dry $[C_2C_1Im][EtSO_4]$, the rupture force of L_1 and L_2 increases with $|\Delta U|$, with a minimum between OCP (black dashed line) and PZC (red dashed line). For $[C_2C_1Im][TFSI]$ and $[N_{1123}][TFSI]$, the rupture force increases over the whole range of potentials owing to the PZC being located at $E < 0$. The rupture force follows a similar trend as the interfacial capacitance, and hence, it appears to be strongly influenced by the charge of graphene, i.e., by the electrostatic interaction between tip and graphene. At the highest applied potential, an additional third layer becomes visible (L_3), which might correspond to the onset of the crowding regime in the EDL.[36]

At 33% RH, the rupture force of L_1 and L_2 achieves a minimum close to the OCP (black dashed line) and increases with potential from OCP (cf. Figure 7D−G). For $[C_2C_1Im][EtSO_4]$, the difference between OCP and PZC (blue dashed line) is negligible. For the hydrophobic ILs, this result suggests the weaker sensitivity of the force to the graphene charge compared to the dry ILs, that is, the hydrophobic WILs with TFSI can screen the surface charge of graphene better than in dry condition.

Analysis of the Interfacial Structure. The response of the solvation layers, i.e., the layer thickness, to potential is shown in Figure 7H−J for dry ILs. For $[C_2C_1Im][EtSO_4]$, there is a significant expansion of the resolved layers at positive and negative ΔU. Above $\Delta U = \pm 0.1$ V, L_1 and L_2 contract. The results for dry $[C_2C_1Im][TFSI]$ show that the change of Δ_2 is qualitatively similar to $[C_2C_1Im][EtSO_4]$, i.e., it increases at small potential around OCP before a contraction is observed (Figure 7I). However, the expansion is not seen for Δ_1 around the OCP. A very small expansion around the OCP followed by a contraction is also observed for L_1 and L_2 in $[N_{1123}][TFSI]$ (Figure 7J).

The qualitatively similar changes of the interfacial layering of dry ILs let us propose similar underlying mechanisms, which are schematically represented in Figure 7O-a−c). That is, the expansion at moderate positive/negative polarizations relative to OCP may be due to (i) the reorientation of the counterions from in-plane to an out-of-plane orientation to compensate the increased surface charge (Figure 7O-a)[46] and/or (ii) the repulsion of co-ions. The compression at higher ΔU reflects the stronger counterion binding (Figure 7O-b). Crowding[36] is possible at the highest applied potentials when additional layers (L_3) are detected (Figure 7O-c). We believe that the large variation of Δ for $[C_2C_1Im][EtSO_4]$ in response to potential changes reflects the dissimilar dimensions of cation and anion (Figure 1C), whereas the cation and anion in $[C_2C_1Im][TFSI]$ and $[N_{1123}][TFSI]$ have similar dimensions, and hence, the change of Δ is comparatively smaller.

The response of the layer thickness to potential is also qualitatively similar for all WILs (Figure 7K−N). Both L_1 and L_2 contract around the OCP for $[C_2C_1Im][EtSO_4]$ (Figure 7K). This contraction is gradual at $\Delta U < 0$ V and more abrupt at $\Delta U > 0$. An increase in ΔU above 0.1 V leads to an expansion. Finally, a contraction is seen at the highest potential. Qualitatively similar results are obtained for $[C_2C_1Im][TFSI]$, $[N_{1123}][TFSI]$ and $[N_{1114}][TFSI]$ (Figure 7L−N), with different extents of contraction and expansion, likely arising from the different molecular structure of the ILs. Comparing to the results of the dry ILs, we note that Δ_1 and Δ_2 decrease in magnitude substantially in the case of $[C_2C_1Im][EtSO_4]$ at 33% RH. In the case of the hydrophobic ILs, in contrast, the expansion of Δ_2 compared to the dry ILs is observed, while Δ_1 for $[C_2C_1Im][TFSI]$ is significantly smaller ($\Delta_1 \sim 2-3$ Å) than at 0% RH.

Overall, there is a significant rearrangement of the interfacial structure in response to the applied potential (also in the presence of water), as the stored charge in the EDL changes with potential. However, these results show that the change of Δ with potential is more intricate for WILs than for dry ILs, reflecting the increased complexity of the interface, since three species—water, counterions, and co-ions—coexist. The contraction of L_1 and L_2 around the OCP, while the rupture force increases, is likely a result of counterion binding at positive and negative polarization. This contraction is gradual at $\Delta U < 0$ V and more abrupt at $\Delta U > 0$ V, reflecting the asymmetric influence of water on the interfacial structure. Note that we observe an expansion around the OCP for the dry ILs, presumably because the ions adopt an out-of-plane configuration to compensate for the increased surface charge, suggesting that water favors charge screening in the WILs. The following expansion at higher ΔU could be related to the rearrangement of the counterions to increase charge density (out-of-plane orientation), the electrostatic repulsion of co-ions and/or hydrophobic interactions upon water enrichment at the interface. Indeed, based on MD simulations on few layer graphene electrodes with imidazolium ILs, water is depleted at low surface charge but greatly enriched at elevated surface charge, and more so near positive electrodes,[18] consistent with the asymmetric response of the WILs. The final contraction at

https://doi.org/10.1021/acsnano.3c01043
ACS Nano 2023, 17, 9347−9360

the highest potential likely reflects counterion binding again. Importantly, the relevance of each of these phenomena should depend on the specific IL composition. For example, the tip could detect water molecules, justifying the decrease of the layer thickness compared to the dry IL. This is expected for $[C_2C_1Im][EtSO_4]$, and it is more likely for $[C_2C_1Im][TFSI]$ than for the two ammonium ILs, which are more hydrophobic; indeed, the decrease of Δ_1 to 2−3 Å for $[C_2C_1Im][TFSI]$ and $[C_2C_1Im][EtSO_4]$ is consistent with the detection of water molecules close to the graphene surface. In the case of the hydrophobic ILs, the larger thickness of L_2 compared to the dry ILs could be associated with a hydrophobic repulsion when water accumulates at the interface.

DISCUSSION

To understand better the charge stored in the EDL of ILs on graphene, we have investigated the influence of water on the capacitance and force−distance curves of five different ILs, one of them is hydrophilic, while the other four ILs have $[TFSI]^-$ or $[FAP]^-$ as anions, which render them much more hydrophobic. A conclusion of this work is that the ESW is not significantly influenced by the presence of water at the graphene/IL interface. This agrees well with MD simulations, which predict that hydrophilic ILs, such as $[C_2C_1Im][EtSO_4]$, can keep water away from electrodes.[20] While this result is unexpected for hydrophobic ILs, it can be justified by the large activation overpotential of water on graphene. Note that the ESW of the selected hydrophobic ILs on gold is indeed reduced abruptly already at 11% RH, which can be associated with the much higher activity of water on gold.

The adsorption of the hydrophobic ILs on graphene leads to significant n-type doping, and this phenomenon is anion-dependent. Previously, a spectroscopic and simulation study had shown that the n-type doping of graphene increases with cation chain length of a series of imidazolium ILs with $[BF_4]^-$.[47] This was justified by (so-called) *electrostatic layering*, i.e., the flat lying alkyl chains prevent anions to approach the unbiased surface, leading to a large potential drop close to the surface, causing n-type doping. Meanwhile, the charge transfer of the adsorbed cations was proven to contribute an opposite but small effect. Based on the electrostatic layering argument, the negligible doping of graphene by $[C_2C_1Im][EtSO_4]$ implies that both $[C_2C_1Im]^+$ and $[EtSO_4]^-$ are present at the interface at OCP, and hence, $[EtSO_4]^-$ reduces (or hinders) the specific adsorption of $[C_2C_1Im]^+$. The hydrogen bonding between $[C_2C_1Im]^+$ and $[EtSO_4]^-$ might be responsible for this.[39] In contrast, the negative shift of the PZC by ILs with $[TFSI]^-$ and $[FAP]^-$ anions (and especially with $[TFSI]^-$) points toward the surface enrichment of the cation even at positive bias; this is consistent with the prominent adsorption peaks in the CVs of these ILs.

Since $C_{IL} \sim \sqrt{\varepsilon}$, the much larger EDL capacitance of $[C_2C_1Im][EtSO_4]$ ($C_{IL} \approx 80\ \mu F\ cm^{-2}$) compared to the hydrophobic ILs ($C_{IL} \approx 5-9\ \mu F\ cm^{-2}$) cannot be justified by its greater dielectric constant alone (27.90 vs 11−12 for the hydrophobic ILs).[28] Note that the uncertainty in the extracted capacitance value of $[C_2C_1Im][EtSO_4]$ is large, as the total capacitance is dominated by the graphene contribution and the assumption of a constant IL capacitance. Smaller values of the IL capacitance are required for smaller hopping parameters of graphene, and if a strong camel-shape capacitance curve is used, values closer to 40 $\mu F\ cm^{-2}$ are obtained. These values still cannot be explained by changes in the dielectric constant alone. In the case of the ILs with $[TFSI]^-$ and $[FAP]^-$ anions, the specific cation adsorption and/or the anion depletion could promote overscreening of positive surface charge[48] and prevent anions to efficiently screen positive surface charge, and thereby, induce the increase of the thickness of the EDL and justify the much smaller C_{IL} compared to $[C_2C_1Im][EtSO_4]$.

Because water molecules favor p-type doping of graphene,[35] the surface enrichment of water should promote the positive shift of the PZC, as seen for $[C_2C_1Im][EtSO_4]$ at 33% RH ($E_{PZC} \sim +0.1$ V). This is supported by AFM measurements, which detect layers of the size of water molecules close to the graphene surface. Importantly, despite the significant change of the interfacial structure inferred from force measurements, the total interfacial capacitance is still dominated by the quantum capacitance of graphene, which implies that C_{IL} remains large, despite the large water content.

Upon water uptake, E_{PZC} shifts to more negative values (from −0.2 to −0.28 V) in $[C_2C_1Im][FAP]$. While analysis of the interfacial structure from force measurements was not possible for this IL due to the attractive force between graphene and surface, the significant drop of the contact angle is consistent with the presence of water close to the graphene surface. Because $[FAP]^-$ is the most hydrophobic anion, it is possible that the interfacial water molecules deplete more $[FAP]^-$ anions away from the graphene surface, which promotes the enrichment of more cations at the surface and n-type doping of graphene. The decrease of C_{int} at positive potentials upon water uptake is thus consistent with the less efficient screening due to anion depletion.

The behavior of the hydrophobic TFSI-ILs with alkylammonium and imidazolium cations is quite different. Here, the presence of water molecules significantly reduces n-type doping of graphene, as the E_{PZC} becomes less negative, and it is even zero for $[C_2C_1Im][TFSI]$. This suggests that more anions and/or water approach the graphene surface compared to 0% RH, and therefore, both the specific adsorption of imidazolium and alkylammonium cations on graphene and the anion depletion are reduced, and thus, screening of positive charge is improved. It is possible that this happens because water molecules preferentially hydrogen bond with TFSI anions compared to the cations.[19] Indeed, the decrease of the layer thickness inferred from force measurements at 33% RH is consistent with water molecules populating the layers close to the graphene surface. Overall, these results support that water uptake improves the screening of graphene's surface charge by the TFSI-ILs with both imidazolium and alkylammonium cations compared to dry conditions, which justifies the observed increase of C_{int} (and C_{IL}) at positive potentials.

Measurements of forces between charged surfaces in dilute electrolytes have served to understand the EDL using Debye−Hückel theory and Poisson−Boltzmann equations. A similar approach has been also applied to ILs, either using AFM or surface force apparatus (SFA). To the best of our knowledge, while long-ranged forces have been revealed by SFA, as will be discussed shortly, most of the AFM force measurements, like the ones reported here, only show a short-range force. As described earlier, the tip force is sensitive to the graphene charge, which is reflected in an electrostatic contribution, to the interfacial layers, where the charge is stored in the liquid, and to the presence of water. Such force has a range of <2 nm, and hence, it is at odds with the long-range forces measured by SFA, including our own SFA measurements.[49,50]

https://doi.org/10.1021/acsnano.3c01043
ACS Nano 2023, 17, 9347−9360

About a decade ago, force measurements by SFA between charged mica surfaces in ILs revealed long-range forces with decay lengths of several nanometers.[50,51] For example, for $[C_2C_1Im][TFSI]$ and $[C_2C_1Im][EtSO_4]$, the decay length is ∼7 and ∼9 nm, respectively.[52] An increase of the water content in equilibrium at 33% RH leads to a prominent decrease of the decay length of $[C_2C_1Im][EtSO_4]$ from ∼9 to ∼2 nm.[49] Because the force responds to a bias potential, it was assumed that it is a long-range electrostatic force.[51] It was then proposed that IL ions are strongly correlated, which causes over 99.99% of ions to bind into overall neutral ion pairs and not participate in charge screening in the EDL. However, measurements of capacitance and ion conductivity contradict the assumption of long-range screening by a small number of free ions.[8,53,54] Despite the disagreement with SFA, our reported AFM measurements do not contradict capacitance (here) and conductivity measurements.

While ion pairs are a conceptually simple construct, in such a concentrated system, one would expect ion pairs to combine into larger neutral aggregates, and even charged aggregates that contribute to screen surface charge.[55,56] Along these lines, an alternative explanation for the long-range force in SFA was proposed.[57] From wide-angle X-ray scattering (WAXS),[57] a phase transformation was reported for several imidazolium ILs, consisting of ions ordering in domains of ∼10 nm over at least 20 h, indicating the formation of large aggregates in the bulk IL. If they were affine to the surface, these domains of large aggregates should naturally lead to a long-range repulsive force with a decay length of ∼10 nm, consistent with SFA force measurements. The work also demonstrated that, over the course of the ordering of the IL, the surface force changes, so that there is a correlation between the evolution of ion ordering in the bulk IL (from WAXS) and the variation of the surface force. Because AFM involves much shorter equilibration times (<1 h) than SFA experiments, it is possible that the long-ranged forces arising from the reorganization of ions in nm-large domains do not have time to develop. Indeed, one study by colloidal probe AFM revealed the presence of such force only when the temperature was increased from 80 to 100 or 120 °C.[58] The characteristics of the long-ranged force being switched on upon an increase in temperature are consistent with an Arrhenius-type phase transformation (i.e., formation of IL aggregates) that requires long equilibration times to happen but becomes measurable by AFM at short equilibration times if the temperature is sufficiently high.

Recently, the EDL of ILs with account of aggregation and gelation was investigated by theory,[59,60] where it was found that the percolating ionic network could also partially screen electrode charge because of the reversible nature of the associations in IL electrolytes. While only the simplest case has been investigated so far, further investigation of aggregation phenomena, and more generally the analogy between electrolytes and polymers in the EDL[61] of ILs could yield insights into the extremely long-ranged interactions, long time scales of relaxation, and highly asymmetric transference numbers.[62]

CONCLUSIONS

In this work, the influence of water on wetting of graphene by five different ILs, their ESW, capacitance, and interfacial structure has been investigated. The differential capacitance displays a V-shape near the PZC of graphene, which is in accordance with the dominance of the quantum capacitance of graphene, as demonstrated by theory. The four hydrophobic ILs lead to a negative potential at the PZC, which indicates the n-type doping of graphene, likely because anions are depleted from the surface and cations are preferentially adsorbed on graphene; this hinders efficient charge screening and decreases the EDL capacitance of the ILs. Theory reveals that the EDL capacitance of the hydrophilic $[C_2C_1Im][EtSO_4]$ is one magnitude larger than that of the four selected hydrophobic ILs. The greater EDL capacitance can be justified by the ability to screen graphene charge more efficiently by $[C_2C_1Im][EtSO_4]$ compared to the ILs with $[TFSI]^-$ and $[FAP]^-$ anions.

The presence of water does not lead to a significant reduction of the ESW of the ILs, although contact angle and AFM force measurements support the presence of water at the liquid/graphene interface. Water uptake also leads to a positive shift of the PZC, except in the case of $[C_2C_1Im][FAP]$. The latter is justified by the more significant depletion of the strongly hydrophobic $[FAP]^-$ anion from the graphene surface by water molecules than in the dry condition, preventing them from screening the surface charge; this can also explain the decrease of the total interfacial capacitance that we observe in EIS experiments. In contrast, the water molecules allow $[TFSI]^-$ anions to approach the surface, thereby justifying the increase of the total interfacial capacitance compared to the dry condition in the range of investigated potentials. Furthermore, the experimentally observed increase of the EDL capacitance of TFSI-ILs agrees with predictions of a satellite peak by theory. In the case of $[C_2C_1Im][EtSO_4]$, the interfacial capacitance is still dominated by the quantum capacitance despite the large water uptake. We also find a decrease in the time constant upon water uptake by the imidazolium ILs, while a subtle increase of the time constant is obtained for the alkylammonium ILs, suggesting that water influences ion−ion interactions in various ways.

AFM force measurements reveal a short-range electrostatic force between tip and graphene and the significant rearrangement of the interfacial layers in response to the applied potential, both in the absence and presence of water, reflecting the variation of the stored charge in the EDL. Finally, we discuss the discrepancy between this short-range force measured by AFM and the reported long-range force detected by SFA in the literature and justify the difference based on the thermally activated aggregation and gelation of ions in highly concentrated electrolytes, supported by both theory and experiments.

MATERIALS AND METHODS

Materials. $[C_2C_1Im][EtSO_4]$ (Sigma-Aldrich, USA, ≥95% purity), $[C_2C_1Im][FAP]$ (EMD Millipore Corporation, USA, ≥98% purity), $[C_2C_1Im][TFSI]$ (Sigma-Aldrich, USA, ≥98% purity), $[N_{1114}][TFSI]$ (Sigma-Aldrich, USA, ≥99% purity) and $[N_{1123}][TFSI]$ (Iolitec, Germany, ≥99%) were purchased. A volume of ∼1.5 mL was dried under vacuum at 50 °C for a week. The ILs (∼1.5 mL) were stored for 1 week in sealed containers at selected relative humidity (RH) to gravimetrically determine the water uptake of the ILs in equilibrium. Relative humidities of 11%, 33% and 44% were maintained constant in the containers with LiCl, $MgCl_2$ and K_2CO_3 saturated solutions, respectively. Single-layer graphene synthesized by chemical vapor deposition and deposited on a silicon oxide substrate was purchased (Graphenea, Spain) and stored under vacuum before use. Graphene on SiO_2 is p-doped due to the interaction with SiO_2 as well as water and oxygen adsorption.[34] Before electrochemical and AFM experiments, graphene was annealed under 450 °C for 4 h in N_2 flow. To examine the quality of graphene, Raman microspectroscopy measure-

https://doi.org/10.1021/acsnano.3c01043
ACS Nano 2023, 17, 9347−9360

ments were collected with a Nanophoton Raman 11 (Nanophoton, Osaka, Japan) microscope using a 532 nm laser. Laser power was set to at least 1 mW, with exposures lasting at least 15 s per spot.

Cyclic Voltammetry. The electrochemical cell consists of a working electrode, which is the graphene sheet (1.89 cm^2), Au wire as a counter electrode, whose surface area is much larger than graphene, thus the capacitance of the counter electrode can be neglected, and an Ag wire as a reference electrode. CVs were measured using a CHI700E potentiostat at 10 mV s^{-1} to characterize the electrochemical window of the ILs. IR compensation was performed to correct the applied potential, with the uncompensated resistance determined by EIS at OCP. For comparison, the CVs were also measured on gold films (25 nm gold films on silicon wafers). The specific capacitance C_s (μF cm^{-2}) was estimated according to

$$\int_{V_1}^{V_2} I(V)dV = 2(V_2 - V_1)C_s mk$$

where k is the scan rate, m is the mass of the active material (single-layer graphene or gold film), and I is the measured current. The calculation was carried out within a potential window ~ ±0.5 V, where the CVs look close to ideal.

EIS Measurements. EIS measurements were conducted in the same setup as the CV, with graphene as working electrode, a gold wire as counter electrode and a silver wire as reference electrode. A Gamry Reference 620 potentiostat was used for EIS measurements. Based on previous studies,[63,64] the sequence of potentials was chosen to go from OCP to positive potentials, followed by relaxation to return to OCP for several hours (ranging from 1.5 to 8 h depending on the IL), and then from OCP to negative potentials with a step of 0.1 V. The impedance measurements at each potential were performed in the frequency range from 0.1 Hz to 1 MHz. The sweeps were performed by applying a sinusoidal potential (10 mV) over a DC voltage. Each applied DC potential was held constant without oscillation for 60 s before measurement. The analysis methods are described in the SI.

Contact Angle Measurements. Contact angles were measured using a Ramé-Hart 250-F1 contact angle goniometer. Graphene samples were placed on the goniometer stage after leveling the stage and calibrating the instrument. The camera was first focused on the front edge of the sample to check the tilting. Then the camera was focused on the tip of the micropipette while making a drop of the IL liquid (~5 μL) and placing it on the surface. The goniometer software was used to capture the images, fit the shape of the droplet, and calculate the liquid volume and contact angle. Each reported contact angle is the average of 10 measurements taken over 10 s.

AFM Force Measurements. Imaging and force measurements were conducted with a JPK (Santa Barbara, CA) atomic force microscope (AFM). AFM tips were cleaned by UV for 20 min prior to the measurement. After annealing, the graphene was immediately mounted into the electrochemical cell. AFM images of the graphene surface were acquired first in tapping mode in air with a backside gold coated tip (BudgetSensors, Sofia, Bulgaria) with a resonant frequency of ~300 kHz. The images were collected at scan rates between 1 and 2 Hz. Following imaging in air, the AFM tip was changed to a contact mode tip (CSC-37 silicon tips from MikroMasch, CA), and graphene samples and tip were immersed in the IL and allowed to equilibrate for 40 min prior to force measurements. Images of the graphene samples immersed in the IL were typically collected in contact mode with sharp Si-tips with a spring constant of ~0.5 N/m and a nominal tip radius ~20 nm, at an applied load of 5 nN and scan rates between 1 and 1.5 Hz. The spring constant was determined by the thermal noise method.[65] The tip is likely slightly negatively charged due to the presence of an oxide layer, which increases the number of cations between the tip and graphene, but this has been ignored in the preceding discussion, since the tip characteristics are the same in all measurements.

CVs measured before and after the AFM experiments at a scan rate of 100 mV/s ensured that contamination and faradaic reactions did not occur during the long duration of the experiments. The volume of the EC cell (~1.35 mL) was filled with the IL to ensure immersion of the counter and reference electrodes. The diameter of the working electrode is ~15.6 mm, resulting in a working electrode area of ~1.89 cm^2. The Au counter (diameter 1 mm) and Ag reference electrodes (diameter 0.5 mm) were sonicated in Milli-Q water and ethanol and dried with dry N_2. The electrochemical potential was applied using a CHI potentiostat. AFM force measurements were obtained at the open circuit potential, positive and negative potentials against an Ag pseudo-reference electrode. The tip velocity was set at 10−20 nm s^{-1}. A total of 64 force curves at each potential were collected from a 500 nm × 500 nm area by dividing the area into 8×8 separate squares and collecting a force curve from each square.

ASSOCIATED CONTENT

Supporting Information

The Supporting Information is available free of charge at https://pubs.acs.org/doi/10.1021/acsnano.3c01043.

AFM image and Raman spectra of single layer graphene on SiO_2; additional CV measurements including CVs of ILs on gold under various relative humidity conditions, adsorption peaks in CVs of ILs on graphene, CVs of 10 mM KCl on graphene and gold, and CVs of ILs on graphene with small windows; EIS data including Nyquist plots, Cole−Cole plots, real capacitance vs frequency and imaginary capacitance vs frequency; calculation methods of interfacial capacitance from EIS measurements, fitted parameters and time constants; additional EIS measurements to determine PZC for the two ammonium ILs; table of water uptake of ILs at different RH; theory for calculation of quantum capacitance and IL capacitance (PDF)

AUTHOR INFORMATION

Corresponding Author

Rosa M. Espinosa-Marzal − *Department of Civil and Environmental Engineering and Department of Materials Science and Engineering, University of Illinois at Urbana-Champaign, Urbana, Illinois 61801, United States;* orcid.org/0000-0003-3442-2511; Email: rosae@illinois.edu

Authors

Qianlu Zheng − *Department of Civil and Environmental Engineering, University of Illinois at Urbana-Champaign, Urbana, Illinois 61801, United States*

Zachary A. H. Goodwin − *Department of Materials, Imperial College London, London SW7 2AZ, United Kingdom; John A. Paulson School of Engineering and Applied Science, Harvard University, Cambridge, Massachusetts 02138, United States;* orcid.org/0000-0003-2760-4499

Varun Gopalakrishnan − *Department of Materials Science and Engineering, University of Illinois at Urbana-Champaign, Urbana, Illinois 61801, United States*

Alexis G. Hoane − *Department of Chemistry, University of Illinois at Urbana-Champaign, Urbana, Illinois 61801, United States*

Mengwei Han − *Department of Civil and Environmental Engineering, University of Illinois at Urbana-Champaign, Urbana, Illinois 61801, United States*

Ruixian Zhang − *Department of Chemistry, University of Illinois at Urbana-Champaign, Urbana, Illinois 61801, United States*

Nathaniel Hawthorne − *Department of Chemistry, Texas A&M University, College Station, Texas 77843, United States*

James D. Batteas − *Department of Chemistry and Department of Materials Science and Engineering, Texas A&M University, College Station, Texas 77843, United States;* orcid.org/0000-0002-6244-5000

Andrew A. Gewirth − *Department of Chemistry, University of Illinois at Urbana-Champaign, Urbana, Illinois 61801, United States;* orcid.org/0000-0003-4400-9907

Complete contact information is available at: https://pubs.acs.org/10.1021/acsnano.3c01043

Author Contributions

R.M.E. and Q.Z. designed the research. Q.Z., Z.A.H.G, V.G., A.G.H., M.H, and R.Z. performed the research. Q.Z., Z.A.H.G, and R.M.E. analyzed data and wrote the paper. J.D.B., N.H., and A.A.G. discussed the data and revised the paper. The manuscript was written through contributions of all authors. All authors have given approval to the final version of the manuscript.

Funding

This material is based upon work supported by the National Science Foundation under grant DMR-1904681, DMR-1904887 and CBET 1916609.

Notes

The authors declare no competing financial interest.

ACKNOWLEDGMENTS

Research was carried out in part in the Materials Research Laboratory Central Research Facilities, University of Illinois.

REFERENCES

(1) Simon, P.; Gogotsi, Y.; Dunn, B. Where do batteries end and supercapacitors begin? *Science* **2014**, *343* (6176), 1210−1211.
(2) Stoller, M. D.; Park, S.; Zhu, Y.; An, J.; Ruoff, R. S. Graphene-based ultracapacitors. *Nano Lett.* **2008**, *8* (10), 3498−3502.
(3) Borenstein, A.; Hanna, O.; Attias, R.; Luski, S.; Brousse, T.; Aurbach, D. Carbon-based composite materials for supercapacitor electrodes: a review. *Journal of Materials Chemistry A* **2017**, *5* (25), 12653−12672.
(4) Verkholyak, T.; Kuzmak, A.; Kornyshev, A. A.; Kondrat, S. Less Is More: Can Low Quantum Capacitance Boost Capacitive Energy Storage? *J. Phys. Chem. Lett.* **2022**, *13* (47), 10976−10980.
(5) Chen, H.; Müller, M. B.; Gilmore, K. J.; Wallace, G. G.; Li, D. Mechanically strong, electrically conductive, and biocompatible graphene paper. *Adv. Mater.* **2008**, *20* (18), 3557−3561.
(6) Zhu, Y.; Murali, S.; Cai, W.; Li, X.; Suk, J. W.; Potts, J. R.; Ruoff, R. S. Graphene and graphene oxide: synthesis, properties, and applications. *Adv. Mater.* **2010**, *22* (35), 3906−3924.
(7) El-Kady, M. F.; Shao, Y.; Kaner, R. B. Graphene for batteries, supercapacitors and beyond. *Nature Reviews Materials* **2016**, *1* (7), 1−14.
(8) Fedorov, M. V.; Kornyshev, A. A. Ionic liquids at electrified interfaces. *Chem. Rev.* **2014**, *114* (5), 2978−3036.
(9) Xu, K. Electrolytes and interphases in Li-ion batteries and beyond. *Chem. Rev.* **2014**, *114* (23), 11503−11618.
(10) González, A.; Goikolea, E.; Barrena, J. A.; Mysyk, R. Review on supercapacitors: Technologies and materials. *Renewable and sustainable energy reviews* **2016**, *58*, 1189−1206.
(11) Ye, J.; Wu, Y. C.; Xu, K.; Ni, K.; Shu, N.; Taberna, P. L.; Zhu, Y.; Simon, P. Charge Storage Mechanisms of Single-Layer Graphene in Ionic Liquid. *J. Am. Chem. Soc.* **2019**, *141* (42), 16559−16563.
(12) Uesugi, E.; Goto, H.; Eguchi, R.; Fujiwara, A.; Kubozono, Y. Electric double-layer capacitance between an ionic liquid and few-layer graphene. *Sci. Rep* **2013**, *3*, 1595.
(13) Xia, J.; Chen, F.; Li, J.; Tao, N. Measurement of the quantum capacitance of graphene. *Nature Nanotechnol.* **2009**, *4* (8), 505−509.
(14) Wood, B. C.; Ogitsu, T.; Otani, M.; Biener, J. First-Principles-Inspired Design Strategies for Graphene-Based Supercapacitor Electrodes. *J. Phys. Chem. C* **2014**, *118* (1), 4−15.
(15) Tran, C. D.; De Paoli Lacerda, S. H.; Oliveira, D. Absorption of water by room-temperature ionic liquids: effect of anions on concentration and state of water. *Appl. Spectrosc.* **2003**, *57* (2), 152−157.
(16) Mele, A.; Tran, C. D.; De Paoli Lacerda, S. H. The structure of a room-temperature ionic liquid with and without trace amounts of water: the role of C[bond]H···O and C[bond]H···F interactions in 1-n-butyl-3-methylimidazolium tetrafluoroborate. *Angew. Chem., Int. Ed. Engl.* **2003**, *42* (36), 4364−4366.
(17) Fazio, B.; Triolo, A.; Di Marco, G. Local organization of water and its effect on the structural heterogeneities in room-temperature ionic liquid/H2O mixtures. *J. Raman Spectrosc.* **2008**, *39* (2), 233−237.
(18) Feng, G.; Jiang, X.; Qiao, R.; Kornyshev, A. A. Water in ionic liquids at electrified interfaces: the anatomy of electrosorption. *ACS Nano* **2014**, *8* (11), 11685−11694.
(19) Budkov, Y. A.; Kolesnikov, A. L.; Goodwin, Z. A. H.; Kiselev, M. G.; Kornyshev, A. A. Theory of electrosorption of water from ionic liquids. *Electrochim. Acta* **2018**, *284*, 346−354.
(20) Bi, S.; Wang, R.; Liu, S.; Yan, J.; Mao, B.; Kornyshev, A. A.; Feng, G. Minimizing the electrosorption of water from humid ionic liquids on electrodes. *Nat. Commun.* **2018**, *9* (1), 5222.
(21) Docampo-Alvarez, B.; Gomez-Gonzalez, V.; Montes-Campos, H.; Otero-Mato, J. M.; Mendez-Morales, T.; Cabeza, O.; Gallego, L. J.; Lynden-Bell, R. M.; Ivanistsev, V. B.; Fedorov, M. V.; Varela, L. M. Molecular dynamics simulation of the behaviour of water in nano-confined ionic liquid-water mixtures. *J. Phys.: Condens. Matter* **2016**, *28* (46), 464001.
(22) Pereira, M. M.; Kurnia, K. A.; Sousa, F. L.; Silva, N. J. O.; Lopes-da-Silva, J. A.; Coutinho, J. A. P.; Freire, M. G. Contact angles and wettability of ionic liquids on polar and non-polar surfaces. *Phys. Chem. Chem. Phys.* **2015**, *17* (47), 31653−31661.
(23) Bordes, E.; Douce, L.; Quitevis, E. L.; Padua, A. A. H.; Costa Gomes, M. Ionic liquids at the surface of graphite: Wettability and structure. *J. Chem. Phys.* **2018**, *148* (19), 193840.
(24) Rilo, E.; Pico, J.; García-Garabal, S.; Varela, L.; Cabeza, O. Density and surface tension in binary mixtures of CnMIM-BF4 ionic liquids with water and ethanol. *Fluid Phase Equilib.* **2009**, *285* (1−2), 83−89.
(25) Sarkar, S.; Pramanik, R.; Ghatak, C.; Setua, P.; Sarkar, N. Probing the Interaction of 1-Ethyl-3-methylimidazolium Ethyl Sulfate ([Emim][EtSO4]) with Alcohols and Water by Solvent and Rotational Relaxation. *J. Phys. Chem. B* **2010**, *114* (8), 2779−2789.
(26) Noack, K.; Leipertz, A.; Kiefer, J. Molecular interactions and macroscopic effects in binary mixtures of an imidazolium ionic liquid with water, methanol, and ethanol. *J. Mol. Struct.* **2012**, *1018*, 45−53.
(27) Hamelin, A. Cyclic voltammetry at gold single-crystal surfaces. Part 1. Behaviour at low-index faces. *J. Electroanal. Chem.* **1996**, *407* (1−2), 1−11.
(28) Weingärtner, H. The static dielectric constant of ionic liquids. *Zeitschrift für Physikalische Chemie* **2006**, *220* (10), 1395−1405.
(29) Friedl, J.; Markovits, I. I.; Herpich, M.; Feng, G.; Kornyshev, A. A.; Stimming, U. Interface between an Au (111) Surface and an Ionic Liquid: The Influence of Water on the Double-Layer Capacitance. *ChemElectroChem.* **2017**, *4* (1), 216−220.
(30) Roling, B.; Drüschler, M.; Huber, B. Slow and fast capacitive process taking place at the ionic liquid/electrode interface. *Faraday Discuss.* **2012**, *154*, 303−311.
(31) Atkin, R.; Borisenko, N.; Drüschler, M.; Endres, F.; Hayes, R.; Huber, B.; Roling, B. Structure and dynamics of the interfacial layer between ionic liquids and electrode materials. *J. Mol. Liq.* **2014**, *192*, 44−54.
(32) Drüschler, M.; Borisenko, N.; Wallauer, J.; Winter, C.; Huber, B.; Endres, F.; Roling, B. New insights into the interface between a single-crystalline metal electrode and an extremely pure ionic liquid: slow interfacial processes and the influence of temperature on

interfacial dynamics. *Phys. Chem. Chem. Phys.* **2012**, *14* (15), 5090−5099.
(33) Uysal, A.; Zhou, H.; Feng, G.; Lee, S. S.; Li, S.; Fenter, P.; Cummings, P. T.; Fulvio, P. F.; Dai, S.; McDonough, J. K.; Gogotsi, Y. Structural Origins of Potential Dependent Hysteresis at the Electrified Graphene/Ionic Liquid Interface. *J. Phys. Chem. C* **2014**, *118* (1), 569−574.
(34) Kang, Y.-J.; Kang, J.; Chang, K.-J. Electronic structure of graphene and doping effect on SiO 2. *Phys. Rev. B* **2008**, *78* (11), 115404.
(35) Du, X.; Guo, H.; Jin, Y.; Jin, Q.; Zhao, J. Electrochemistry Investigation on the Graphene/Electrolyte Interface. *Electroanalysis* **2015**, *27* (12), 2760−2765.
(36) Kornyshev, A. A. Double-layer in ionic liquids: paradigm change? *J. Phys. Chem. B* **2007**, *111* (20), 5545−5557.
(37) Goodwin, Z. A.; Feng, G.; Kornyshev, A. A. Mean-field theory of electrical double layer in ionic liquids with account of short-range correlations. *Electrochim. Acta* **2017**, *225*, 190−197.
(38) Wu, Y. C.; Ye, J.; Jiang, G.; Ni, K.; Shu, N.; Taberna, P. L.; Zhu, Y.; Simon, P. Electrochemical Characterization of Single Layer Graphene/Electrolyte Interface: Effect of Solvent on the Interfacial Capacitance. *Angew. Chem., Int. Ed. Engl.* **2021**, *60* (24), 13317−13322.
(39) Zhang, Q. G.; Wang, N. N.; Yu, Z. W. The hydrogen bonding interactions between the ionic liquid 1-ethyl-3-methylimidazolium ethyl sulfate and water. *J. Phys. Chem. B* **2010**, *114* (14), 4747−4754.
(40) Jurado, L. A.; Kim, H.; Rossi, A.; Arcifa, A.; Schuh, J. K.; Spencer, N. D.; Leal, C.; Ewoldt, R. H.; Espinosa-Marzal, R. M. Effect of the environmental humidity on the bulk, interfacial and nanoconfined properties of an ionic liquid. *Phys. Chem. Chem. Phys.* **2016**, *18* (32), 22719−22730.
(41) Zhang, Y.; Brar, V. W.; Girit, C.; Zettl, A.; Crommie, M. F. Origin of spatial charge inhomogeneity in graphene. *Nat. Phys.* **2009**, *5* (10), 722−726.
(42) Samaddar, S.; Yudhistira, I.; Adam, S.; Courtois, H.; Winkelmann, C. B. Charge Puddles in Graphene near the Dirac Point. *Phys. Rev. Lett.* **2016**, *116* (12), 126804.
(43) Elbourne, A.; McDonald, S.; Voïchovsky, K.; Endres, F.; Warr, G. G.; Atkin, R. Nanostructure of the Ionic Liquid−Graphite Stern Layer. *ACS Nano* **2015**, *9* (7), 7608−7620.
(44) Jurado, L. A.; Espinosa-Marzal, R. M. Insight into the Electrical Double Layer of an Ionic Liquid on Graphene. *Sci. Rep* **2017**, *7* (1), 4225.
(45) Feng, G.; Chen, M.; Bi, S.; Goodwin, Z. A. H.; Postnikov, E. B.; Brilliantov, N.; Urbakh, M.; Kornyshev, A. A. Free and Bound States of Ions in Ionic Liquids, Conductivity, and Underscreening Paradox. *Physical Review X* **2019**, *9* (2), 021024.
(46) Fedorov, M. V.; Georgi, N.; Kornyshev, A. A. Double layer in ionic liquids: The nature of the camel shape of capacitance. *Electrochem. Commun.* **2010**, *12* (2), 296−299.
(47) Velpula, G.; Phillipson, R.; Lian, J. X.; Cornil, D.; Walke, P.; Verguts, K.; Brems, S.; Uji-i, H.; De Gendt, S.; Beljonne, D.; Lazzaroni, R.; Mali, K. S.; De Feyter, S. Graphene Meets Ionic Liquids: Fermi Level Engineering via Electrostatic Forces. *ACS Nano* **2019**, *13* (3), 3512−3521.
(48) Bazant, M. Z.; Storey, B. D.; Kornyshev, A. A. Double layer in ionic liquids: overscreening versus crowding. *Phys. Rev. Lett.* **2011**, *106* (4), 046102.
(49) Espinosa-Marzal, R. M.; Arcifa, A.; Rossi, A.; Spencer, N. D. Ionic Liquids Confined in Hydrophilic Nanocontacts: Structure and Lubricity in the Presence of Water. *J. Phys. Chem. C* **2014**, *118* (12), 6491−6503.
(50) Espinosa-Marzal, R. M.; Arcifa, A.; Rossi, A.; Spencer, N. D. Microslips to "Avalanches" in Confined, Molecular Layers of Ionic Liquids. *J. Phys. Chem. Lett.* **2014**, *5* (1), 179−184.
(51) Gebbie, M. A.; Valtiner, M.; Banquy, X.; Fox, E. T.; Henderson, W. A.; Israelachvili, J. N. Ionic liquids behave as dilute electrolyte solutions. *Proc. Natl. Acad. Sci. U. S. A.* **2013**, *110* (24), 9674−9679.
(52) Han, M.; Espinosa-Marzal, R. M. Electroviscous Retardation of the Squeeze Out of Nanoconfined Ionic Liquids. *J. Phys. Chem. C* **2018**, *122* (37), 21344−21355.
(53) Goodwin, Z. A. H.; Kornyshev, A. A. Underscreening, overscreening and double-layer capacitance. *Electrochem. Commun.* **2017**, *82*, 129−133.
(54) Chen, M.; Goodwin, Z. A. H.; Feng, G.; Kornyshev, A. A. On the temperature dependence of the double layer capacitance of ionic liquids. *J. Electroanal. Chem.* **2018**, *819*, 347−358.
(55) McEldrew, M.; Goodwin, Z. A. H.; Zhao, H.; Bazant, M. Z.; Kornyshev, A. A. Correlated Ion Transport and the Gel Phase in Room Temperature Ionic Liquids. *J. Phys. Chem. B* **2021**, *125* (10), 2677−2689.
(56) McEldrew, M.; Goodwin, Z. A. H.; Bi, S.; Bazant, M. Z.; Kornyshev, A. A. Theory of ion aggregation and gelation in super-concentrated electrolytes. *J. Chem. Phys.* **2020**, *152* (23), 234506.
(57) Han, M.; Kim, H.; Leal, C.; Negrito, M.; Batteas, J. D.; Espinosa-Marzal, R. M. Insight into the Electrical Double Layer of Ionic Liquids Revealed through Its Temporal Evolution. *Advanced Materials Interfaces* **2020**, *7* (24), 2001313.
(58) Hjalmarsson, N.; Atkin, R.; Rutland, M. W. Switchable long-range double layer force observed in a protic ionic liquid. *Chem. Commun. (Camb)* **2017**, *53* (3), 647−650.
(59) Goodwin, Z. A. H.; McEldrew, M.; Pedro de Souza, J.; Bazant, M. Z.; Kornyshev, A. A. Gelation, clustering, and crowding in the electrical double layer of ionic liquids. *J. Chem. Phys.* **2022**, *157* (9), 094106.
(60) Goodwin, Z. A. H.; Kornyshev, A. A. Cracking Ion Pairs in the Electrical Double Layer of Ionic Liquids. *Electrochim. Acta* **2022**, *434*, 141163.
(61) Goodwin, Z. A. H.; McEldrew, M.; Kozinsky, B.; Bazant, M. Z. Theory of Cation Solvation and Ionic Association in Nonaqueous Solvent Mixtures. *PRX Energy* **2023**, *2* (1), 013007.
(62) McEldrew, M.; Goodwin, Z. A. H.; Molinari, N.; Kozinsky, B.; Kornyshev, A. A.; Bazant, M. Z. Salt-in-Ionic-Liquid Electrolytes: Ion Network Formation and Negative Effective Charges of Alkali Metal Cations. *J. Phys. Chem. B* **2021**, *125* (50), 13752−13766.
(63) Lockett, V.; Sedev, R.; Ralston, J.; Horne, M.; Rodopoulos, T. Differential Capacitance of the Electrical Double Layer in Imidazolium-Based Ionic Liquids: Influence of Potential, Cation Size, and Temperature. *J. Phys. Chem. C* **2008**, *112* (19), 7486−7495.
(64) Masuyama, K. Electrochemistry of room temperature ionic Liquids with applications to electrospray propulsion. *Ph.D. Thesis*, Massachusetts Institute of Technology, Cambridge, MA, May 13, 2016.
(65) Hutter, J. L.; Bechhoefer, J. Calibration of atomic-force microscope tips. *Review of scientific instruments* **1993**, *64* (7), 1868−1873.

https://doi.org/10.1021/acsnano.3c01043
ACS Nano 2023, 17, 9347−9360